Distal Enhanced Sedimentation From Volcanic Plumes: Insights From the Secondary Mass Maxima in the 1992 Mount Spurr Fallout Deposits

Julia Eychenne, Alison Rust, Katharine Cashman, Wolfram Wobrock

AGU PUBLICATIONS

JGR

Journal of Geophysical Research: Solid Earth

RESEARCH ARTICLE
10.1002/2017JB014412

Key Points:
- Areas of secondary mass maximum (ASMM) in tephra fallout deposits do not always result from preferential settling of ash <125 μm in size relative to coarser grain sizes
- Bimodal total grain size distributions of eruptions can affect the sedimentological pattern of the tephra fallout deposits
- Topography-induced perturbations of the wind field generate turbulence above rough terrain, which can accelerate the transfer of particles toward the low atmospheric layers

Supporting Information:
- Supporting Information S1

Correspondence to:
J. Eychenne,
julia.eychenne@uca.fr

Citation:
Eychenne, J., Rust, A. C., Cashman, K., & Wobrock, W. (2017). Distal enhanced sedimentation from volcanic plumes: Insights from the secondary mass maxima in the 1992 Mount Spurr fallout deposits. *Journal of Geophysical Research: Solid Earth*, *122*, 7679–7697. https://doi.org/10.1002/2017JB014412

Received 5 MAY 2017
Accepted 22 SEP 2017
Accepted article online 26 SEP 2017
Published online 21 OCT 2017

Distal Enhanced Sedimentation From Volcanic Plumes: Insights From the Secondary Mass Maxima in the 1992 Mount Spurr Fallout Deposits

Julia Eychenne[1,2], Alison C. Rust[2], Katharine V. Cashman[2], and Wolfram Wobrock[3]

[1]Laboratoire Magmas et Volcans, Université Clermont Auvergne-CNRS-IRD, OPGC, Aubière, France, [2]School of Earth Sciences, University of Bristol, Bristol, UK, [3]Laboratoire de Météorologie Physique, Université Clermont Auvergne-CNRS, OPGC, Aubière, France

Abstract Some tephra fallout deposits show an increase of mass and thickness at distances from the source >100 km (areas of secondary mass maximum, ASMM) which demonstrates distal enhanced sedimentation from volcanic plumes. We explore development of the ASMMs during the 1992 August and September Mount Spurr eruptions, USA, by combining field data on the spatial distribution of mass and grain size with (1) simulations of individual particle settling through a homogeneous and horizontally stratified atmosphere and (2) mesoscale models of the three-dimensional wind field that include the effect of the underlying topography. The crosswind and downwind variations of deposit characteristics indicate that the increase of sedimentation at the ASMMs is not formed solely because of preferential settling of small ash particles (<125 μm), as commonly assumed in aggregation models. Instead, ASMM grain sizes correspond to the fine modes of the bimodal total grain size distributions. There also appears to be a link between the ASMM and the topography: the mass local minima occur across the windward flank of 2 km high mountain ranges, while the ASMMs spread on the leeward flank. Mesoscale models of the three-dimensional wind field show vertical oscillations in the wind over mountainous regions which may enhance mechanisms of en masse sedimentation (aggregation, hydrometeor formation, and particle boundary layers), as well as strong spatial variations of the horizontal wind field in the lower troposphere. Our study demonstrates the importance of using grain size, as well as mass, data to constrain the complex processes responsible for particle sedimentation from volcanic plumes.

1. Introduction

Explosive volcanic eruptions inject large amounts of fragmented material (tephra) into Earth's atmosphere, which are subsequently dispersed by the winds. Dispersion and sedimentation of tephra plumes through the atmosphere can disturb aviation airspace (Kueppers et al., 2014; Webley, 2015) and destroy crops and infrastructure on the ground and cause adverse respiratory effects (e.g., Horwell & Baxter, 2006; Jenkins et al., 2015; Wilson et al., 2015). A critical aspect of volcanology is thus to understand the physical processes controlling the atmospheric path of tephra, which depends strongly on the plume depletion during dispersion, that is, the fallout of tephra to the ground (e.g., Bursik et al., 1992; Sparks et al., 1992). New field and experimental evidence demonstrates that the sedimentation mechanisms controlling plume depletion can be complex. In particular, the fall of individual particles through the atmosphere at their terminal velocity only partially describes the settling behavior of tephra (e.g., Del Bello et al., 2017), while additional collective sedimentation processes such as aggregation (e.g., Bagheri et al., 2016; Taddeucci et al., 2011) and en masse collapse of gravitational instabilities (e.g., Carazzo & Jellinek, 2012, 2013; Durant et al., 2009; Manzella et al., 2015) can be significant.

Sedimentation of tephra on the ground forms cone- to sheet-like fallout deposits that thin exponentially over several hundreds of kilometers (e.g., Pyle, 1989; Walker, 1981). However, several sheet-like tephra fallout deposits show a local increase of mass and thickness at distal locations (Brazier et al., 1983; Brown et al., 2012; Carey & Sigurdsson, 1982; Hildreth & Drake, 1992; Sarna-Wojcicki et al., 1981), hereafter referred to as areas of secondary mass maximum (ASMM). There are clear ASMMs in fallout deposits from the 1932 eruption of Quizapu, Chile (Hildreth & Drake, 1992; Larsson, 1937), the 18 May 1980 Mount St. Helens eruption, USA (Sarna-Wojcicki et al., 1981), the 3 June 1991 Unzen eruption, Japan (Watanabe et al., 1999), the August and September 1992 Spurr eruptions, USA (McGimsey et al., 2001), and an ~9.75 ka Chaitén eruption, Chile

(Watt et al., 2015). There are also complex distal depositional patterns sometimes considered to be ASMMs, such as in the 1991 Hudson, Chile (Scasso et al., 1994), 1991 Pinatubo, Philippines (Wiesner et al., 2004), and 2008 Chaiten, Chile, fallout deposits (Watt et al., 2009). The presence of ASMMs in fallout deposits indicates that enhanced deposition of tephra can occur locally after the plume has spread to great distances (>100 km). This demonstrates unambiguously that sedimentation of tephra is not solely controlled by the fall of individual particles through a constant atmosphere. Understanding the mechanisms producing ASMMs can thus bring valuable insights into particle sedimentation processes and improve physical models of volcanic plume dispersion and depletion.

Here we explore a range of processes that can affect the dispersion and sedimentation of volcanic plumes and assess their importance in the formation of ASMMs. We focus on the 1992 August and September eruptions of Mount Spurr, Alaska, which produced exceptionally well documented fallout deposits and conspicuous ASMMs at distances greater than 150 km from vent (McGimsey et al., 2001). Processes of ash deposition for both eruptions have previously been modeled by Durant and Rose (2009) assuming single spherical particles falling through an atmosphere considered as a stack of homogeneous horizontal layers. They showed that this simple approach overestimates the settling distance of fine ash compared to the observed grain size in the deposits. They explain the discrepancy using thermodynamic modeling of the September plume, which indicates that ice-coated ash hydrometeors could have formed near the tropopause, allowing for later sublimation and en masse sedimentation from the plume base (Durant & Rose, 2009). The September Spurr ASMM has also been reproduced numerically using the tephra transport and sedimentation models FALL3D and Ash3d (Folch et al., 2010; Mastin et al., 2016), both of which include ash aggregation. Confirmation of complex ash deposition during the Spurr eruptions comes from shape analyses and terminal fall velocity measurements in the laboratory on a tephra sample from the distal end of the ASMM of the August deposit, which show that particles with a wide range of shape, density, and terminal velocity settled at a single location (Riley et al., 2003).

Here we extend these studies using crosswind and downwind variations of both mass and grain size within the deposits. Like Durant and Rose (2009), we use both numerical simulations of individual particle settling through a simplified and horizontally stratified atmosphere; our approach differs in exploring the effects of particle shape on settling velocity. We also model the three-dimensional wind field at the mesoscale to assess the impact of the underlying topography on atmospheric turbulence and particle transport. We then use these results to assess the effects of different scenarios of distal enhanced sedimentation on the characteristics (location and grain size) of the ASMMs. We conclude that in contrast to existing models of particle aggregation, all grain sizes present in the plume at the relevant distance from vent are contributing to the mass increase on the ground and that both the total grain size distribution (TGSD) generated at the vent and topography-induced perturbations of the wind field may play important, and often ignored, roles in controlling depositional patterns of tephra.

2. Models of Aggregation, ASMM Formation, and Impact on Deposit Trends

2.1. Aggregation Models for ASMM Formation

The first conceptual and semiempirical model of ASMM formation was developed to explain the trends in the fallout deposit from the 18 May 1980, Mount St. Helens (MSH) eruption, where a clear ASMM is located ~300 km from the vent (Sarna-Wojcicki et al., 1981). Bimodal grain size distributions were also observed in the ASMM, which suggested that the two features were related (Brazier et al., 1983; Carey & Sigurdsson, 1982). Early numerical simulations of the dispersion and sedimentation of the MSH plume reproduced the lateral mass variation of the deposit along the axis by assuming that all fine ash (i.e., particles <63 μm in size) aggregated in clusters falling individually at a velocity of 0.35 m/s (Carey & Sigurdsson, 1982). Based on this study, and the real-time observations of 250 to 500 μm clumps falling from the MSH plume ~400 km from vent (Sorem, 1982), Brazier et al. (1983) suggested that the fine grain size mode was generated by ash settling as aggregates that formed the ASMM. Brazier et al. (1983) extended this analysis to other fall deposits and concluded that grain size bimodality in individual samples from fall deposits is due to a single process—aggregation—and suggested that ASMMs would be observed in more fallout deposits if they were documented more distally.

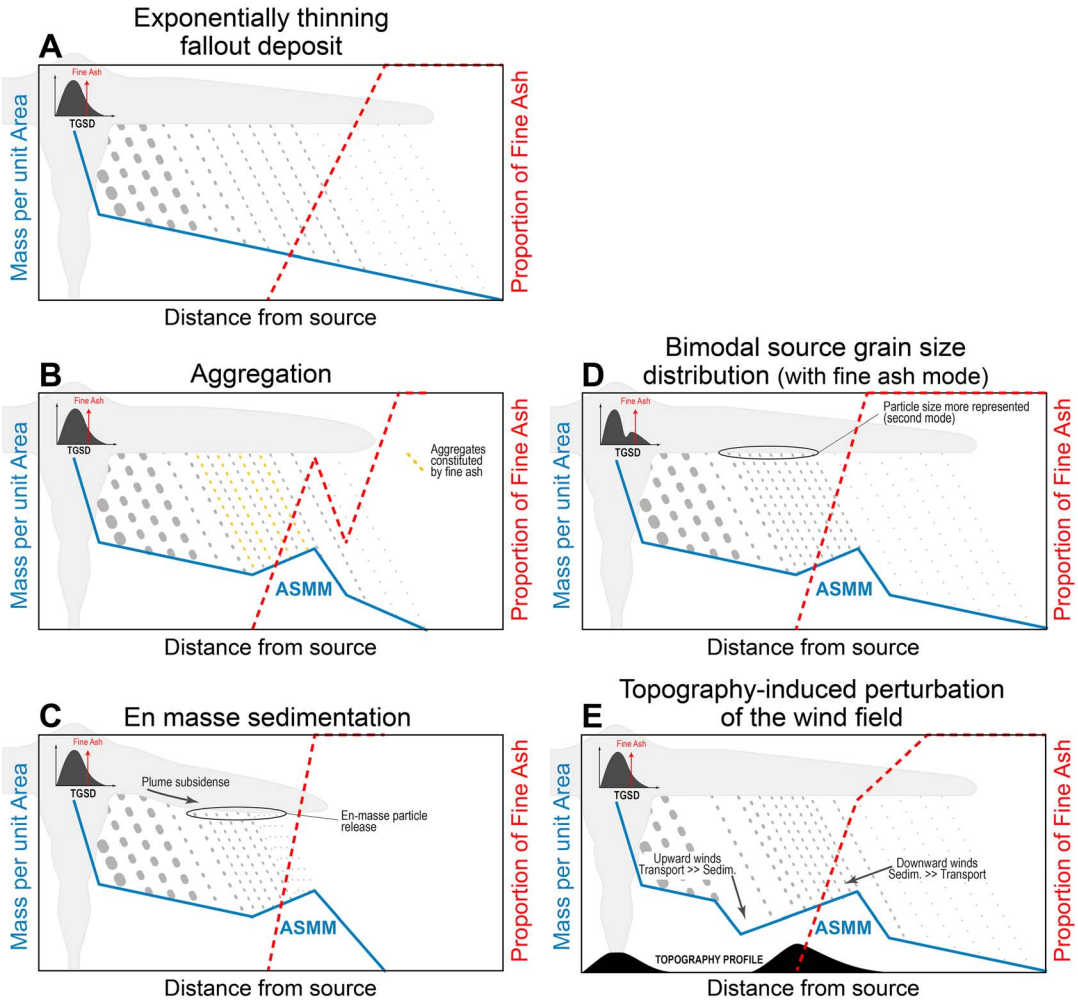

Figure 1. Schematic of the variations of mass and fine ash content (i.e., particles <63 μm in size) in fallout deposits expected for different atmospheric and source conditions, and different sedimentation behaviors. The blue and red dotted lines represent the variations of MpuA (left axis) and proportion of fine ash (right axis), respectively. The cartoons in the background represent schematically the settling of particles from a spreading volcanic plume.

The idea that aggregation causes ASMMs is now widespread (e.g., Brown et al., 2012). We illustrate this conceptual model by examining the expected variations of both mass per unit area (MpuA) and the proportion of fine ash (<63 μm, i.e., >4Φ as $\Phi = -log_2(particle\ diameter\ in\ millimeters)$) along the fallout deposit axis (Figure 1). In the ideal context of (1) a unimodal source grain size distribution and (2) individual particle sedimentation from a volcanic plume spreading in a constant wind field, an exponentially thinning deposit is produced (Figure 1a). The proportion of fine ash increases linearly with distance and reaches 100% after the plume is entirely depleted in particles coarser than 63 μm. Under the same conditions, aggregation will create an ASMM only if the aggregates generated in the dispersing plume are restricted to a narrow range of size and density that causes them to fall in a limited area rather than spreading through the deposit (Figure 1b).

The inferred link between aggregation and ASMM formation has led to a practice of using mass distributions (MpuA) within deposits to calibrate models of ash aggregation (e.g., Carey & Sigurdsson, 1982; Cornell et al., 1983; Costa et al., 2010; Folch et al., 2010; Mastin et al., 2016). The September deposit of the Spurr eruption has been a particular focus of such studies in recent years. For example, Mastin et al. (2016) use the Spurr deposit to calibrate an empirical ash aggregation scheme, which attributes all fine ash and 50% of the 3Φ (125 μm) size class to aggregates with a narrow Gaussian size distribution (tests standard deviation of 0, 0.1, 0.2, and 0.3 Φ and means from 1.9 to 3.1Φ) and density of 600 kg/m^3. The best fit to the Spurr deposit, which corresponds to an aggregate size distribution with mean = 2.4Φ and standard deviation = 0.1Φ,

substantially underestimates MpuA along the dispersal axis; the same approach to the 1980 MSH deposit strongly underestimates the distal ash load. A sophisticated wet aggregation scheme was introduced by Costa et al. (2010) and applied to the September Spurr deposit by Folch et al. (2010). The best fit of the simulations to MpuA data from the Spurr deposit is for aggregates with component grains with a fractal dimension of 3 (which is the maximum possible value, corresponding to a size distribution that can completely fill a space) and falling velocity of 0.29 times that of a nonporous sphere of the same diameter as the aggregate. This scheme predicts that only 23, 22, 32, 54, and 45% of the particles 125, 63, 32, 15.6, and 8 μm in size will form aggregates in the 2Φ class (250–500 μm) for this eruption, and so some very fine ash falls as individual particles. The inclusion of this aggregation scheme in the model generates a prominent ASMM and substantially improves agreement with the overall set of deposit MpuA data points, although the misfit for some individual locations is worse with aggregation.

Observational evidence shows that both in the field (Bagheri et al., 2016; Bonadonna et al., 2002; Sorem, 1982; Taddeucci et al., 2011) and in the laboratory (Gilbert & Lane, 1994; James et al., 2002, 2003; van Eaton et al., 2012), wet and dry clustering mechanisms actually generate a wide range of aggregate types, shapes, sizes, and densities. Although there is no reason to expect that all aggregate types will be produced during a single eruption (e.g., Brown et al., 2012), generation of only a single class of aggregates (in terms of size, density, and shape) is also highly unlikely (e.g., Bonadonna et al., 2002). In fact, models that assume aggregates of a single (Folch et al., 2010) or very limited (Mastin et al., 2016) range in size and/or density should produce an abrupt and distal increase of MpuA that correlates directly with an increase in the proportion of fine ash (Figure 1b). Moreover, where not all particles in a given size class are included in the aggregates, sedimentation should resume as settling of individual particles, and the transition from aggregate to individual particle should produce an abrupt decrease of MpuA, closing the ASMM (Figure 1b). From a grain size perspective, particles that are included in aggregates should show some premature deposition relative to their calculated settling velocities, and these particle sizes should be in the deposit beyond the ASMM in accordance with single-particle settling (but in diminished quantity compared to without aggregation). In particular, the proportion of fine ash should decrease abruptly beyond the ASMM limit of aggregation-assisted settling before increasing with distance (Figure 1b). Consequently, in ASMMs produced only by model aggregation processes, the proportion of fine ash should follow the mass variations within the ASMM. Assessing the accuracy of such models thus requires comparison not only of modeled and observed MpuA but also of grain size data at individual locations in the deposit. Importantly, a recent study shows that incorporation of grain size data into an inversion scheme also improves mass estimates, even when aggregation is not important (White et al., 2017).

2.2. Additional Contributions to ASMM Formation

As illustrated above, ASMMs not only provide insights into the distal dispersion and sedimentation behavior of volcanic plumes but can also improve our understanding of ash aggregation. Here we turn the question around, to examine mechanisms of ASMM formation that may be independent of aggregation. Interestingly, numerical simulations of the September 1992 Spurr eruption produce an ASMM at about the right distance from source without including aggregation, although in this case the modeled ASMM is deficient in mass relative to the observations (Folch et al., 2010). Here the ASMM forms as a consequence of the total grain size distribution (TGSD) of the eruption, which is bimodal because of enrichment in fine ash (Rose & Durant, 2009). Interestingly, other deposits with bimodal TGSDs also show ASMMs, including that of 1980 MSH, where bimodality, aggregation, and ASMMs were originally linked (Brazier et al., 1983; Carey & Sigurdsson, 1982). In this case, the grain size bimodality of the deposit results from mixing of ash contributions from two different sources (fine-grained coblast and coarser vent-derived plumes) (Eychenne et al., 2015). These examples highlight mechanisms other than aggregation alone that can both enhance distal tephra sedimentation and produce ASMMs.

To illustrate the effects of different enhanced sedimentation mechanisms on ASMM formation and deposit-wide patterns of grain size variations, we consider how the ideal depositional pattern in Figure 1a would be affected by (1) variations in initial conditions and (2) different dispersion and sedimentation scenarios. The case of a bimodal TGSD is shown in Figure 1d. Here simplistically, each grain size mode is assumed to produce a mass mode at the depositional distance corresponding to the settling of individual grains of that size; the maximum size mode will therefore create the ASMM. In this example, the proportion of fine ash should increase smoothly with distance at a rate that depends on the rate of grain size change for $\Phi > 4$. En

masse sedimentation is another suggested mechanism of premature fine ash deposition (Carazzo & Jellinek, 2013; Manzella et al., 2015) and ASMM formation (Durant & Rose, 2009; Durant et al., 2008). The latter has been attributed to microphysical processes of ice coating ash in a moist atmosphere followed by sublimation or melting of the hydrometeors, which can trigger rapid en masse sedimentation of the gravitationally unstable lower portion of the cloud (Durant & Rose, 2009; Durant et al., 2009). En masse sedimentation should cause a rapid release of all particle sizes locally present in the plume to form an ASMM with a wide size range and a rapid increase in the proportion of fine ash coincident with the ASMM (Figure 1c). A final mechanism for ASMM formation is topography-induced perturbation of the wind field that increases upward wind velocities on windward sides of mountains and downward wind velocities on lee sides (Jiang & Doyle, 2004; Watt et al., 2015). Such perturbations of wind velocities can retain tephra in suspension on the windward sides of mountains while enhancing tephra sedimentation on the lee sides (Poulidis et al., 2017; Watt et al., 2015). In this case, we would expect the deposited mass of tephra to decrease rapidly upwind of an ASMM, for the ASMM to be located downwind of a topography high, and for the proportion of fine ash to increase within the ASMM (Figure 1e).

3. Background on the 1992 Mount Spurr Eruptions and Field Data

Mount Spurr is an ice-capped, andesitic stratovolcano located 130 km west of Anchorage in the southern part of the Alaska Range. After 10 months of gradually increasing seismic activity, three subplinian eruptions occurred in 1992 at the satellite flank vent of Crater Peak, on 27 June, 18 August, and 16–17 September. Each eruption lasted for 3.5 to 4 h and generated small volume pyroclastic density currents (PDCs) (Miller et al., 1995) and eruptive columns rising to ~14 km above sea level (asl) observed by radar (Rose et al., 2001, 1995). The August and September eruptions were observed in detail (McGimsey et al., 2001; Miller et al., 1995; Rose et al., 2001; Schneider et al., 1995). The 18 August eruption started at 16:42 Alaska Daylight Time (ADT) and waned after 20:00 ADT (Rose et al., 2001). The September event started at 00:03 ADT on 17 September and lasted until ~03:40 ADT (McGimsey et al., 2001; Rose et al., 2001). Satellite infrared (IR) images indicate that during the 30 to 40 h following the start of the eruption, the September plume advected downwind more quickly than the August one, with average speeds of 39 and 16 m/s, respectively (Schneider et al., 1995).

Narrow (30 to 50 km wide) and elongated fallout deposits with dense-rock equivalent volumes of 14 and 15×10^6 m^3 were produced by the August and September eruptions (McGimsey et al., 2001). The deposits extend toward the east southeast and east northeast, respectively, across the Cook Inlet Basin and the eastern mountain ranges (Chugach and Talkeetna Mountains; Figure 2). The ASMMs appear at distances greater than 150 km from vent, a distance at which a clear minimum of MpuA is reached (Figure 2). The proximal deposits contain two types of basaltic andesite clasts—tan and gray pumice—making up a total juvenile content $>$90% (Neal et al., 1995). Each deposit consists of a lower tephra layer rich in tan pumices (60–80%) comprising more than two thirds of the thickness and an upper layer dominated by gray pumices (90% in the August deposit and 65% in the September deposit) representing one third of the thickness (Gardner et al., 1998). Tan and gray pumices differ in their density (1.5 ± 0.2 and 2.1 ± 0.3 g/cm^3, respectively, for clasts 16–4 mm in size) and their vesicularity (41.7 ± 8.0% and 23.0 ± 9.6%) (Gardner et al., 1998). Distal ash from site 44 in the August deposit located 265 km from source (Figure 2) is dominated by particles with 20–40% vesicularity containing plagioclase and pyroxene microlites; smaller microlite-rich glass shards comprise 44% of the studied sample (Riley et al., 2003).

The MpuA of tephra was carefully measured by U.S. Geological Survey (USGS) researchers throughout the fallout deposits up to 400 km from vent during the week following each eruption (Figure 2) (McGimsey et al., 2001). There were no reports of observations of aggregates falling during the eruptions or preserved within the deposits (McGimsey et al., 2001). The grain size of several samples (27 in the August deposit and 21 in the September deposit, Figure 2) was analyzed by sieving and laser diffraction (Durant & Rose, 2009; McGimsey et al., 2001; Rose et al., 2001). We used the grain size data from McGimsey et al. (2001) and Durant and Rose (2009), except for August sample 44 whose grain size data come from Rose et al. (2001); the grain size distribution reported in Durant and Rose (2009) for this sample is inconsistent with the regional trend and measurements in Rose et al. (2001) and Riley et al. (2003). The TGSDs were reconstructed by Durant and Rose (2009) and are bimodal with fine modes between 3 and 5Φ (125–32 μm; Figure 3).

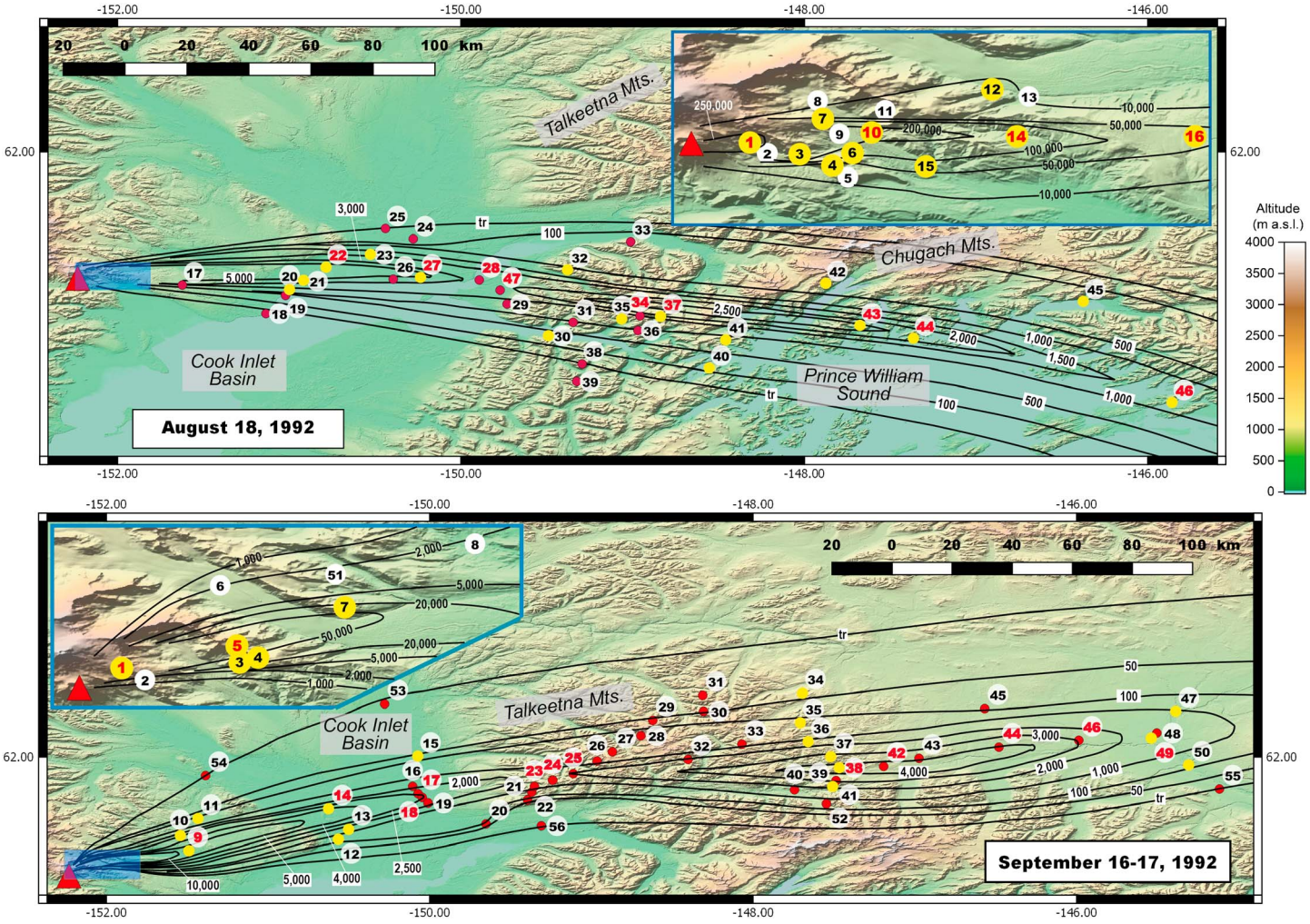

Figure 2. Maps of the tephra fall deposits from the 18 August and 16–17 September 1992 Mount Spurr eruptions, Alaska, showing the locations where the MpuA of tephra deposited was measured (numbered dots) and the isomass lines (black curves) in g/m^2 as drawn by the USGS (McGimsey et al., 2001). The yellow dots represent sites where the deposit was also sampled and the grain size measured. The red sample numbers indicate those that we designate as on axis.

4. Simulation Methods

4.1. Simulations of Individual Particle Settling

We simulate the sedimentation of individual particles through the atmosphere in the meteorological conditions of the 18 August and 16–17 September 1992 using the theoretical settling scheme of Ganser (1993) for nonspherical particles. This scheme is increasingly applied in numerical models of volcanic plume dispersion and sedimentation, including the model NAME of the London Volcanic Ash Advisory Center (e.g., Beckett et al., 2014, 2015). It is different than the Durant and Rose (2009) model that used a drag coefficient after Brown and Lawler (2003) suitable for spherical particles only.

Here the particle Reynolds number (*Re*), drag coefficient (*Cd*), and terminal fall velocity (*Vt*), are expressed as follows:

$$\mathrm{Re} = \frac{(Vt\, D\, \rho_a)}{\mu_a} \tag{1}$$

$$Cd = \frac{24}{\mathrm{Re}\, K_1}\left(1 + 0.1118(\mathrm{Re}\, K_1 K_2)^{0.6567}\right) + \frac{0.4305\, K_2}{1 + \frac{3305}{\mathrm{Re}\, K_1 K_2}} \tag{2}$$

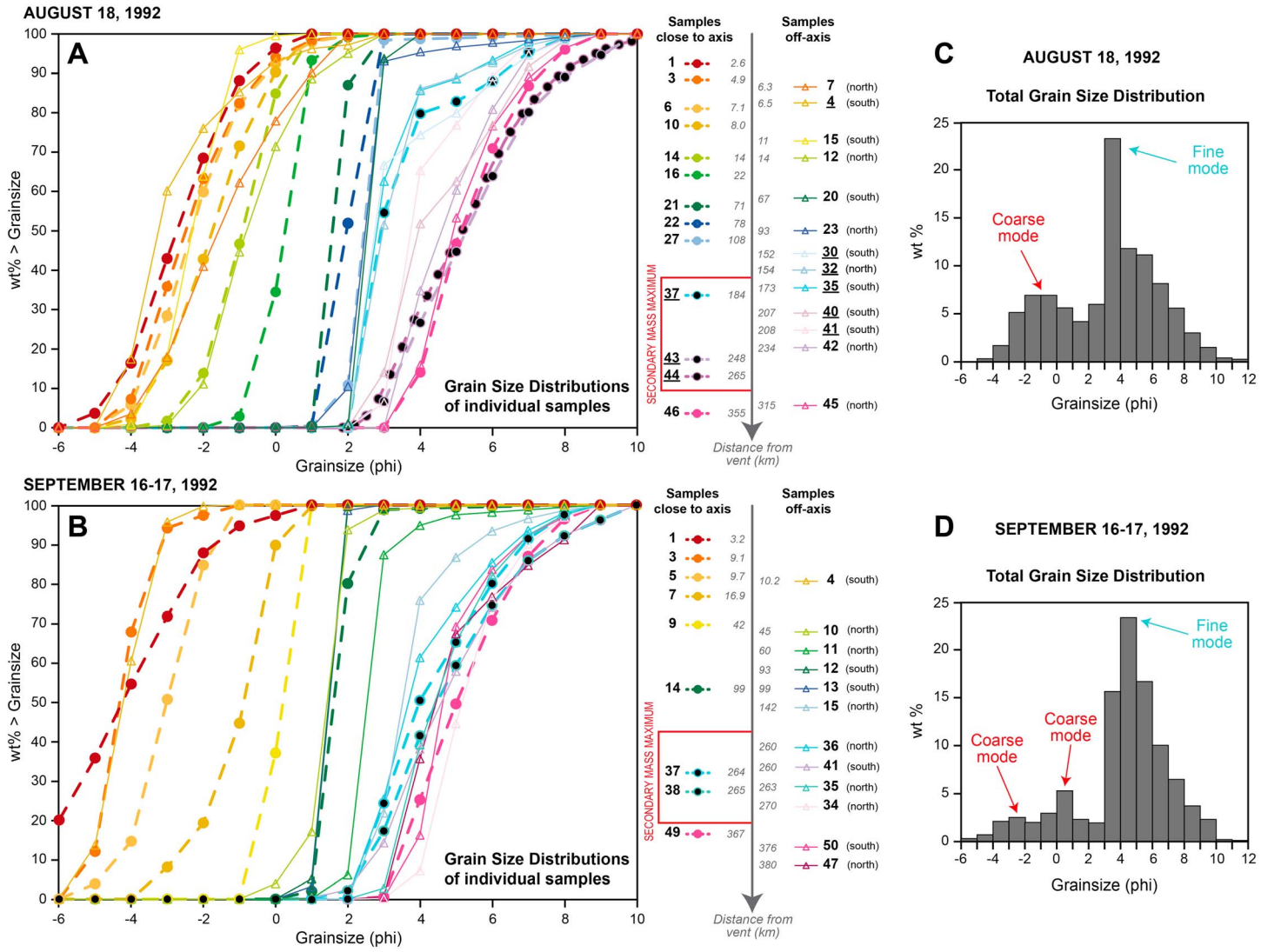

Figure 3. Cumulative grain size distributions of samples from the (a) 18 August and (b) 16–17 September 1992 Mount Spurr fallout deposits. The distribution curves are color coded by their distance from vent (see legends on the right of the plots). The filled and open symbols represent samples located close to and off the deposit axis, respectively. The samples located in the ASMMs are highlighted by black symbols on the plots. The samples underlined on the right legends have bimodal grain size distributions. (c and d) Total grain size distributions of the 18 August and 16–17 September 1992 Mount Spurr fallout deposits, respectively. TGSDs are after Durant and Rose (2009).

$$Vt = \left(\frac{4\,g\,D\left(\rho_p - \rho_a\right)}{3\,Cd\,\rho_a}\right)^{1/2}, \tag{3}$$

where D is the particle diameter, ρ_a the density of the atmosphere, μ_a the dynamic viscosity of the atmosphere, and ρ_p the density of the particle. K_1 and K_2 are Ganser's shape factors, defined as

$$K_1 = \frac{3}{1 + 2\,\psi^{-0.5}} \tag{4}$$

$$K_2 = 10^{\left[1.8148\,(-\log\psi)^{0.5743}\right]}, \tag{5}$$

where ψ is the 3-D sphericity of the particle.

Sedimentation is simulated from the height of plume dispersion (12 km for both eruptions) (Neal et al., 1995; Rose et al., 2001), which corresponds roughly to the altitude of the tropopause (Rose et al., 2001). The troposphere is divided into 1 km thick layers, in which temperature (T, in kelvin), pressure (P), ρ_a, and μ_a are assumed constant. These parameters are calculated following the International Standard Atmosphere model, using an exact solution to the hydrostatic equation for a column of air, the perfect gas law, and the Sutherland law:

$$T = T_0 - L\,h \tag{6}$$

$$P = P_0 \left(\frac{T}{T_0}\right)^{5.256} \tag{7}$$

$$\rho_a = \frac{P}{R\,T} \tag{8}$$

$$\mu_a = \frac{1.458\times10^{-6}\,T^{3/2}}{T + 110.4}, \tag{9}$$

where T_0 and P_0 are the temperature and pressure at sea level (288.2 K and 101.29×10^3 Pa, respectively), L is the lapse rate for the troposphere (6.5 K/km), h is the altitude, and R is the gas constant for air (287 $m^2\ s^{-2}\ K^{-1}$). Given that Re depends on Vt and on the air properties, Re, Cd, and Vt are calculated iteratively in each atmospheric layer. Vt of a particle thus varies with the altitude (Figures S2c and S2d in the supporting information). Particles are advected horizontally by the wind (Figures S2a and S2b in the supporting information), assuming a constant wind speed and direction in each atmospheric layer and neglecting the vertical component of the wind. Similar to Durant and Rose (2009), we implemented observed horizontal wind data in the simulations using atmospheric soundings collected at Anchorage International Airport at the time closest to the eruption time: 16:00 ADT on 18 August (42 min before the start of the August eruption) and 04:00 ADT on 17 September 1992 (4 h after the start of the September eruption) (Figure S3 in the supporting information).

We simulate the sedimentation of tan and gray pumices, 16 mm to 4 μm in size, with different values of sphericity (see Figure S4 in the supporting information for examples of shapes covered by the range of sphericity explored). Based on density profiles observed in many tephra fallout deposits (Bonadonna & Phillips, 2003; Cashman & Rust, 2016; Eychenne & Pennec, 2012), we assume that the density of tan and gray pumices increases linearly with grain size in Φ between $\Phi = -4$ (16 mm), where ρ_p is taken as 1.5 and 2.1 g/cm^3 for tan and gray pumices, respectively, and $\Phi = 3$ (125 μm), where the density reaches the solid density (ρ_p = 2.6 g/cm^3 for both pumice types) and remains constant (Figure S5 in the supporting information). The threshold grain size for the change in density trend is taken at 125 μm by comparison to the densities of particles from the 2006 Tungurahua fallout deposit (Eychenne & Pennec, 2012), which has a similar composition and microlite content to the Spurr pumices (Wright et al., 2012). The effect of a different density profile has also been explored (see Figures S5 and S6 in the supporting information).

4.2. Mesoscale Modeling of the Atmospheric Wind Field

The complex 3-D wind field is simulated at the mesoscale with the National Center for Atmospheric Research (NCAR) Clark-Hall cloud-scale model (Clark et al., 1996). This model has been used to simulate fire events (Coen, 2013), aircraft-damaging turbulence phenomena (Clark et al., 2000), rainfall development (Thielen et al., 2000), and microphysical processes accompanying cloud seeding (Wobrock et al., 2001). The meteorological model is nonhydrostatic and uses the an-elastic form of the continuity equation. It comprises the prognostic equations for wind field, temperature, water vapor, and all forms of cloud/precipitation hydrometeors. A special feature of the model is the use of a terrain-following vertical coordinate, which allows simulation of detailed airflow over complex and steep terrain (Clark, 2003). To initialize the model and to force its

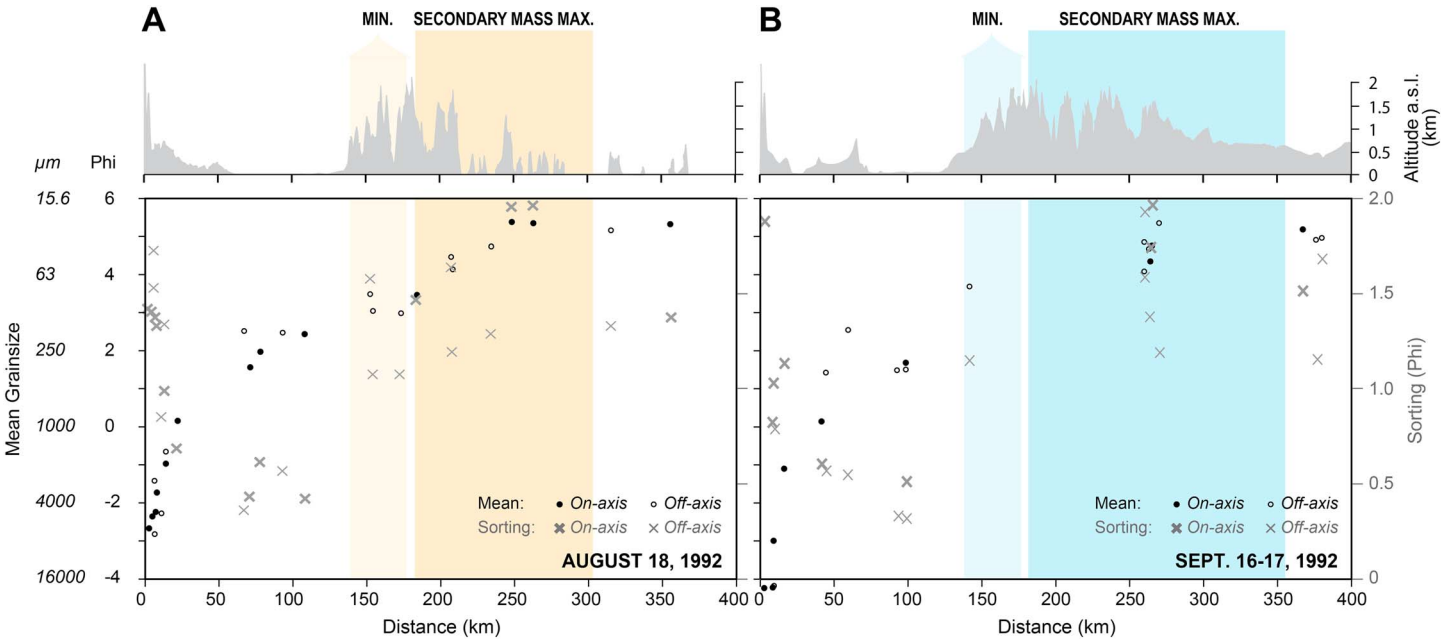

Figure 4. Variations of the mean (left axis) and sorting (akin to standard deviation; right axis) parameters of the bulk (i.e., non-deconvolved) grain size distributions of samples from the (a) 18 August and (b) 16–17 September 1992 Mount Spurr fallout deposits. The topography profiles along the deposit axis are represented, and on- and off-axis samples are distinguished. Mean and sorting are defined after Folk and Ward (1957).

lateral boundaries, the atmospheric fields of wind, temperature, humidity, and pressure were taken from the European Centre for Medium-Range Weather Forecasts (ECMWF)-ERA-interim database for the 18 August and 17 September 1992. The NCAR Clark-Hall cloud-scale model accounts for topography-induced buoyancy perturbations of the stratified atmosphere, which can create regions of turbulence in the upper troposphere and lower stratosphere (Eckermann & Preusse, 1999) and alter the wind field locally in the low atmospheric layers (Jiang & Doyle, 2004).

5. Results

5.1. Grain Size and Mass Variations in the 1992 Mount Spurr Fallout Deposits

The fallout grain size distributions follow similar spatial trends in the August and September deposits (Figures 3 and 4). The mean size decreases consistently with distance from vent, with the samples close to the deposit axis showing a coarser mean than the off-axis samples (Figure 4). The deposit becomes better sorted (the sorting parameter σ decreases) to ~50 km from vent. Samples are extremely well sorted between ~50 and 100 km from vent (Figures 3 and 4), across the area corresponding to the wide valley of the Cook Inlet Basin (Figures 2 and 4). Beyond 100 km, σ increases due to an enrichment of the deposit in fine ash (Figure 4). Individual samples with bimodal grain size distributions are observed in the August deposit (Figure 3a) at variable distances from vent; they are not restricted to the ASMM. No bimodal samples are observed in the September deposit, where the sampling was sparser. The bimodal distributions are deconvolved as a coarse and a fine subpopulation using DECOLOG 5.0 (Bellotti et al., 2010; Caballero et al., 2014) (Figure S1 in the supporting information).

The August and September fallout deposits are characterized by a distal increase in mass with an amplitude of ~2,300 and 3,400 g/m^2, respectively, corresponding to the ASMMs (Figure 5). After reaching a minimum 140 to 160 km from vent in the August deposit and 140 to 170 km from vent in September, the MpuA attains a secondary maximum between 170 and 300 km from vent in the August deposit and between 180 and 350 km from vent in September. In both deposits, the mass minimum occurs across the windward flank of a 2 km high mountain range (Chugach and Talkeetna Mountains; Figure 2), while the maximum spreads across the leeward flank (Figures 5a and 5b).

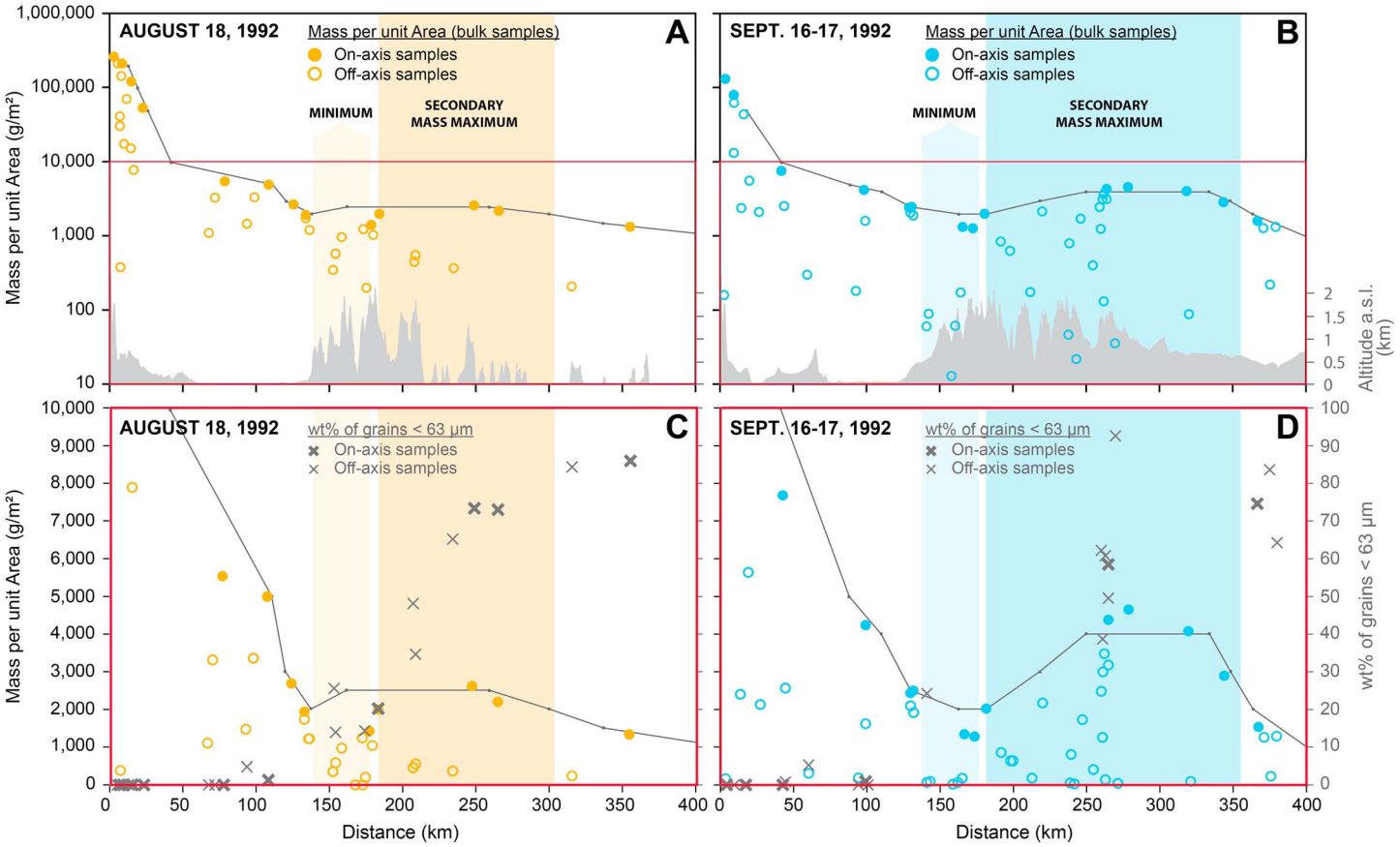

Figure 5. Variation of MpuA with distance from vent, within the (a and c) 18 August and (b and d) 16–17 September 1992 Mount Spurr fallout deposits. The topography profiles along the deposit axes are represented in Figures 5a and 5b. Figures 5c and 5d are expanded plots (red boxes) of Figures 5a and 5b and represent the proportion of fine ash (grains finer than 63 μm) on the right axis (gray crosses). Minima and maxima in the MpuA profiles are highlighted in the plots and determined from the on-axis MpuA variations, with the minima and maxima taken as the areas where MpuA < 1500 g/m^2 and MpuA $> 2{,}000$ g/m^2, respectively. The thin gray lines represent the along the axis linear interpolation of the isomass lines as drawn by McGimsey et al. (2001) and represented in Figure 2.

The fallout deposits lack fine ash (<63 μm) to ≤140 km from vent (Figures 5c and 5d), a distance that corresponds to the foothills of the Chugach and Talkeetna Mountain ranges, where fine ash is first found on the ground. Beyond this location, the proportion of fine ash increases steadily (although with some scatter) with distance, across both the local minima and the ASMMs (Figures 5c and 5d). The proportion of ash <125 μm follows the same trend as the fine ash (<63 μm; Figure 6) and is thus not spatially correlated with the MpuA variations or ASMMs. The proportion of ash <63 μm starts to increase just before the local mass minima, about 100 km closer to the vent than the ASMMs. While MpuA decreases away from the ASMMs (both downwind and crosswind), the proportion of ash <63 μm (and <125 μm) keeps increasing downwind, with no systematic crosswind trend. This indicates that the distal increase in sedimentation causing the ASMMs does not result from preferential settling of ash <63 μm (or <125 μm) compared to coarser grain sizes, in contrast to predictions of aggregation models for ASMM formation (see section 2 and Figure 1b).

5.2. Settling Behavior of Individual Particles

For sphericity values ranging from 0.9 to 0.6, the settling model for individual particles reproduces the mean of the unimodal grain size distributions over the first 100 km of the fallout deposits (Figure 6). The density difference between tan and gray pumices makes relatively little difference to the modeled deposition. A break in slope in the grain size trend with distance is observed at ~50 km from vent in both the field and modeled data. The absence of fine ash on the ground in this area is consistent with this model prediction. In the August deposit, the settling model also explains the coarse subpopulations of the bimodal samples between 100 and 250 km from vent (Figure 6a). The fine ash observed in the deposits (as part of a fine subpopulation in the August bimodal distributions or as part of the unimodal distributions), in contrast, appears much closer to

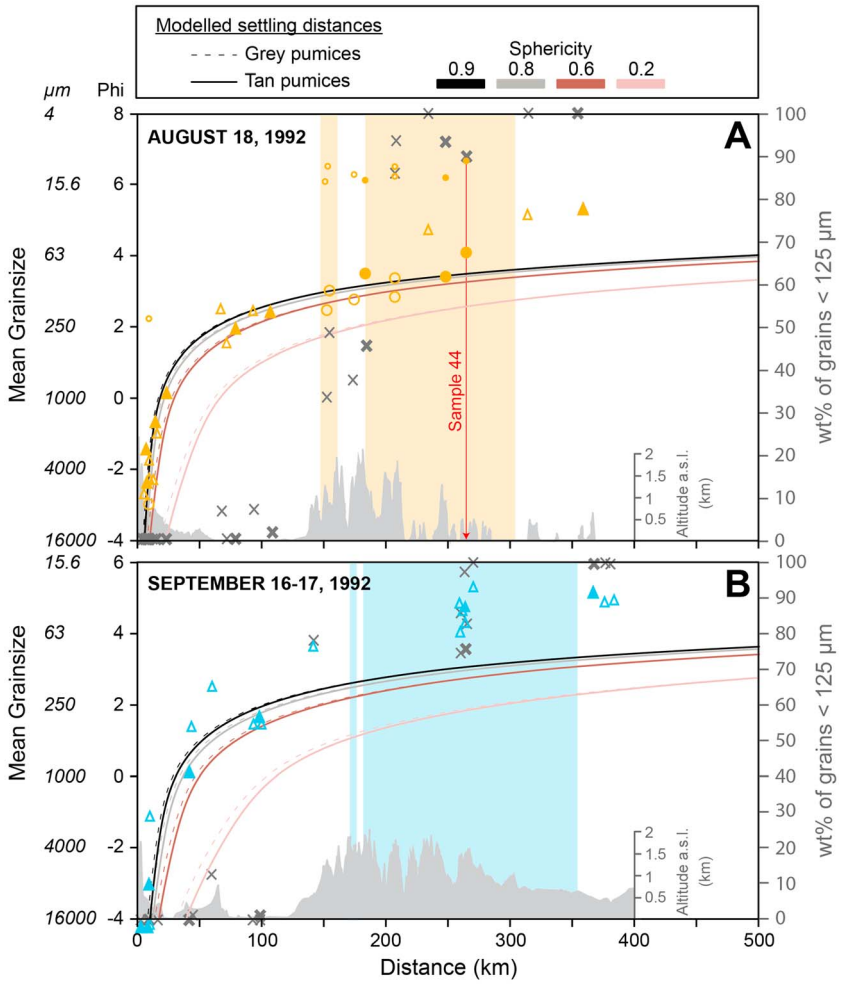

Figure 6. Comparison of simulated versus observed grain size variation in the (a) 18 August and (b) 16–17 September 1992 Mount Spurr fallout deposits. The mean (after Folk & Ward, 1957) of unimodal samples (triangles), as well as coarse (circles) and fine subpopulations (dots) deconvolved from the bimodal distributions, are represented. The on-axis samples (Figure 2) are represented as closed symbols. The curves represent the settling distances of individual particles of various shapes in the local wind field at the time of the eruptions, for tan (continuous lines) and gray pumices (dashed lines). The gray crosses represent the proportion of ash $<$125 μm in size (right axis), with on-axis samples as bold crosses. The topography profiles along the deposit axes are represented, as well as the secondary minima and maxima in mass (same representation as in Figure 5).

the vent than model predictions for nonspherical particles (Figure 6), concurring with the findings of Durant and Rose (2009) based on spherical particles. Our simple modeling approach does not account for turbulence and mesoscale motions that would help the finest particles to travel even farther (Beckett et al., 2015). Although the scarcity of grain size data in the September deposit (Figure 6b) makes it more difficult to assess the capacity of the model to reproduce the field data, we can safely infer that, as with the August case, the model of individual particle settling explains well the field sedimentation pattern for grains larger than ~100 μm.

5.3. Three-Dimensional Atmospheric Wind Field

The wind fields modeled by our mesoscale simulations of the atmosphere during the August and September Spurr eruptions reveal complex 3-D patterns (Figures 7 and S9 in the supporting information). The wind field is strongly affected by topography, with strong vertical oscillations generated by the steep topographic variations characteristic of the mountainous regions of Alaska (Figures 7a and 7b). The vertical oscillations propagate to the stratosphere, creating a highly turbulent troposphere mostly located above the topography. Between 2 and 4 km asl, the horizontal wind field is also variable, with wind channeled toward the north

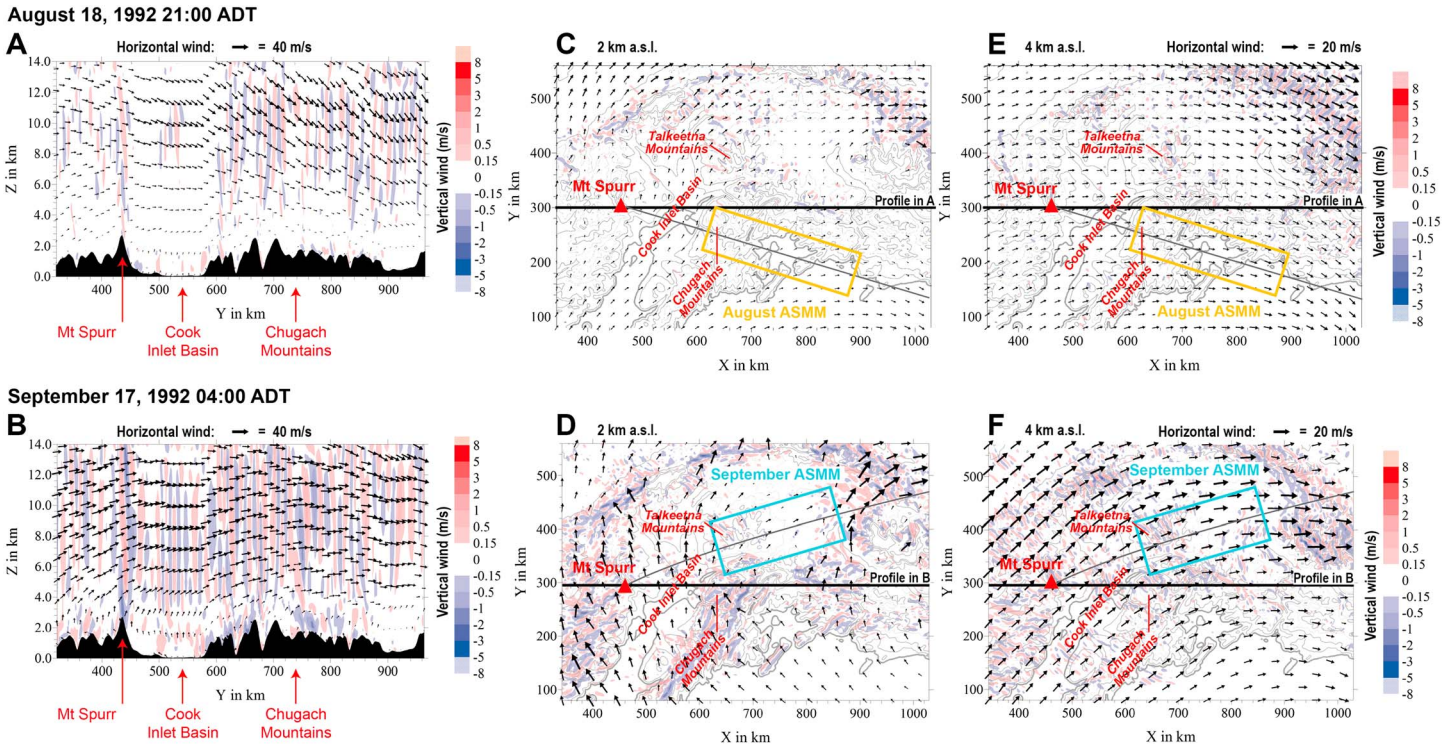

Figure 7. Horizontal (arrows) and vertical (colored areas) wind patterns in the Alaska region downwind of Mount Spurr on 18 August and 17 September 1992, about 4 h after the eruptions started. The wind field is simulated at the mesoscale with the NCAR Clark-Hall cloud-scale model (Clark et al., 1996) using meteorological data from the ECMWF-ERA-interim database. (a and b) Vertical profiles along a west to east cross section through the mountains. (c and d) Maps of the wind pattern at 2 km asl. (e and f) Maps of the wind pattern at 4 km asl. The arrow length and direction represent the speed and *xy* direction of the horizontal component of the wind, respectively. The vertical component of the wind is color coded (see legend), with positive and negative velocities corresponding to upward and downward winds, respectively. The scales for vertical and horizontal wind velocities are the same in Figures 7c and 7d than Figures 7e and 7f. The black and gray lines in Figures 7c–7f represent the east-west traverse represented in profiles (Figures 7a and 7b) and the plume trajectories, respectively. Additional maps representing the wind field at 6 and 8 km asl are presented in Figure S9 in the supporting information.

and northeast in the Cook Inlet Basin and a decrease of the wind speed in the basin west of the Talkeetna mountains (Figures 7c–7f). The September wind field (Figures 7b, 7d, and 7f) is characterized by higher velocities (both vertical and horizontal) than in August, which produces a more turbulent atmosphere. Strong contrasts in horizontal wind velocities in the low troposphere (2 to 4 km asl) are manifested as moderate winds in the Cook Inlet Basin and stagnant areas on the lee side of the Talkeetna mountains (Figures 7b and 7d).

6. Discussion

6.1. Sedimentation Behavior During the Mount Spurr Eruptions

The results of our individual particle settling simulations show that during the Mount Spurr eruptions, ash coarser than 100 μm settled predominantly as individual grains (Figure 6) and was progressively depleted from the plume, leading to an increased proportion of fine ash depositing with distance (Figures 3, 5, and 6). A different type of settling mechanism appears to control the sedimentation of fine ash, which reached the ground much closer to the vent than predicted by individual particle settling (Figure 6), as has been documented in a number of other fallout deposits (e.g., Brazier et al., 1983; Engwell & Eychenne, 2016; Rose & Durant, 2009). As discussed above, numerous processes can explain the observed accelerated transfer of fine ash toward the ground, including aggregation (e.g., Brown et al., 2012; Rose & Durant, 2011; Taddeucci et al., 2011; van Eaton et al., 2012) and other collective sedimentation behaviors such as en masse settling in convective instabilities (Carazzo & Jellinek, 2012; Manzella et al., 2015), hydrometeor-enhanced sedimentation (Durant & Rose, 2009; Durant et al., 2009), and entrainment of fine ash in the wake of settling coarser

grains (Del Bello et al., 2017; Di Muro et al., 2008; Eychenne et al., 2015; Lovell & Rose, 1991). But does the accelerated sedimentation of fine ash cause the formation of the ASMMs in the Spurr fallout deposits?

To answer this question, we compare the simplified depositional patterns illustrated in Figure 1 to observations of mass and grain size distributions in the two Spurr deposits. Importantly, there is no apparent correlation between mass and proportion of fine ash within the Spurr ASMMs (Figures 5 and 6), as would be expected if a size-selective sedimentation process (i.e., enhancing preferentially the settling of fine ash) had caused the distal deposition increase (see section 2 and Figure 1b). Instead, we observe a gradual enrichment in fine ash with distance that initiates just before the mass minima and continues beyond the ASMMs, which reflect a local MpuA increase (Figures 5 and 6). These data suggest that the mechanism responsible for the increased settling affected the sedimentation of both fine ash and coarser particles in a way that modulated the distance and rate at which all the suspended material reached the ground (Figures 4 and 5). We thus conclude that while enhanced fine ash sedimentation processes might have been occurring during the Spurr eruptions, we find no evidence that they produced aggregates with a unique set of characteristics that would have been necessary to trigger the ASMM formation. To constrain the origin(s) of the ASMM and explain the observed decoupling of MpuA and proportion of fine ash, we explore alternative processes affecting particle sedimentation, including (1) changes in horizontal wind velocity at the tropopause during the course of the eruption, (2) the heterogeneity of particle size, shape, and density documented within the ASMM, (3) the bimodality of the source grain size, and (4) complex 3-D wind patterns related to topography-induced perturbations.

6.2. Effect of Horizontal Wind Variations

Fallout deposits represent accumulation of material integrated over the duration of tephra emission. Atmospheric conditions change through time and can thus modify the settling distance of similar material (settling velocity) emitted at different times. This alone can complicate the lateral mass variations of fallout deposits.

Satellite images of downwind spreading of the August plume show that during the first 40 h of dispersion, the plume front traveled more than 2,000 km at an average speed of 16 m/s (Schneider et al., 1995). The detached plume passed over the sampling area (~400 km extent) in less than 20 h (Schneider et al., 1995). The elongated and narrow shape of the fallout deposit (Figure 2) suggests a high wind speed at the altitude of dispersion. A high-velocity layer (25 to 27 m/s) was located at an altitude of about 11 km asl at 16:00 ADT on 18 August (42 min before the eruption started; Figure S3 in the supporting information). It weakened (to 14–16 m/s) but persisted to 04:00 ADT on the morning of 19 August (~11 h after the eruption started) and strengthened again (to 20–25 m/s) by 16:00 ADT on the same day (~23 h after the eruption started). Simulations using the weakest wind profile (04:00 ADT on 19 August) show a significant impact of wind changes on particles finer than 63 μm (Figure S7 in the supporting information). Compared to transport in the 18 August 16:00 ADT wind field, 63 μm and 30 μm individual particles would settle ~60 and 250 km closer to the vent, respectively, at the lower wind speeds (Figure S7 in the supporting information). At 21:11 ADT, ~4.5 h after the eruption started and ~1 h after it stopped, satellite infrared (IR) images show a plume still connected to the vent extending ~400 km toward the southeast, with an optically opaque core indicating high particle concentrations and/or presence of material coarser than 15 μm in diameter (Rose et al., 2001; Schneider et al., 1995). This indicates that substantial deposition must have occurred while the winds weakened, which could explain some of the fine ash within the depositional area.

To explore whether the change in wind velocity could have produced the ASMM, we add observations from September, which also occurred at the time of a high-velocity wind layer. The wind speed averaged 37 m/s at an altitude of about 12 km at 04:00 ADT on 17 September (~4 h after the eruption started); by 16:00 ADT on the same day (~16 h after the eruption started) wind speeds persisted at 30 m/s but at altitudes that decreased 10 to 12 km (Figure S3 in the supporting information). The plume front ultimately traveled more than 3,500 km at an average speed of 39 m/s and the detached plume passed over the sampling area in less than 10 h (Schneider et al., 1995). We assume that such small wind changes had very little effect on the transport of the September plume within the depositional area and cannot explain the formation of the ASMM in this deposit. From this we conclude that the August ASMM may also require additional depositional mechanism(s).

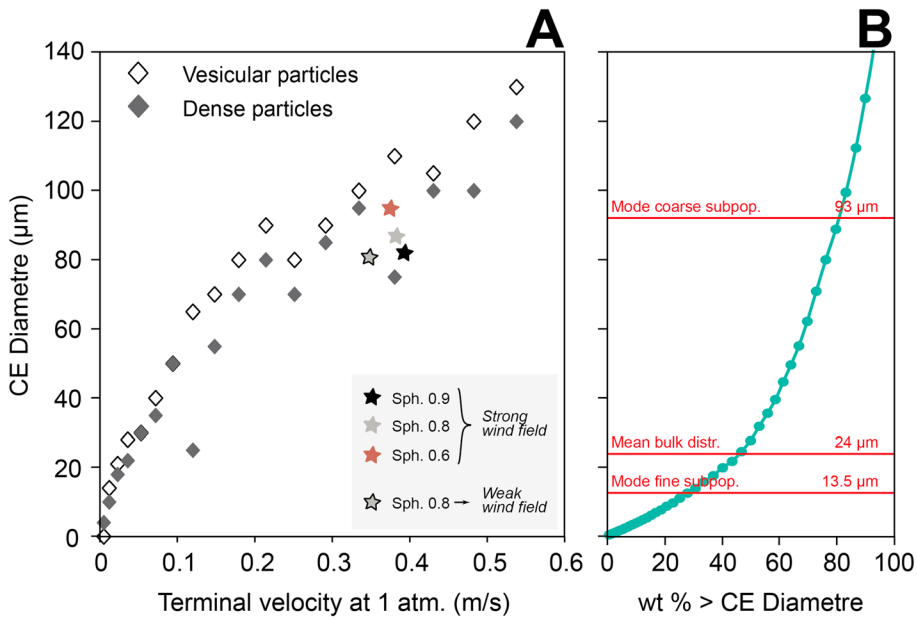

Figure 8. (a) Mean circle-equivalent (CE) diameter of dense (filled diamonds) and vesicular particles (open diamonds) measured in the *Vt* groups identified within tephra sample 44 (Figure 2) of the 18 August 1992 Mount Spurr fallout deposit (data after Riley et al., 2003). The stars represent theoretical *Vt* at sea level (equivalent conditions to the laboratory) for the particles predicted to reach the ground at the location of sample 44 (265 km from vent) by our individual particle settling scheme for different sphericity values in the strong wind field of August 18 16:00 ADT. For a sphericity of 0.8, *Vt* at sea level was also recalculated for particles expected to reach the location of sample 44 in a weak wind field (August 19 04:00 ADT wind profile; see Figure S3). (b) Cumulative grain size distribution of sample 44 (after Rose et al., 2001), including the mean of the bulk grain size distribution and the modes of the coarse and fine subpopulations (Figure S1 in the supporting information).

6.3. Effect of Particle Characteristics

Pyroclasts transported in volcanic plumes are more texturally and morphologically complex than depicted in our settling model, which could affect the distal sedimentation pattern. Fully characterizing the diversity of texture and shape in a tephra sample, and determining the effect of these variations on the settling behavior of the particles, is challenging. Riley et al. (2003) proposed an original approach by measuring, in the laboratory, the settling velocity (*Vt*) of particles from August sample 44 (Riley et al., 2003; Rose et al., 2001), which was collected on axis at a distance of 265 km from vent in Wells Bay, that is, at the distal end of the ASMM (Figures 2, 3, and 6). They used a Roller air elutriation device, which sorts particles into *Vt* groups by modulating the air flow rate injected in a tube holding the sample. Riley et al. (2003) distinguished vesicular from dense grains and measured the size and shape of representative grains in each *Vt* group (Figure 8a).

The *Vt*s measured in sample 44 span a wide range of velocities corresponding to particles ranging from 4 to 130 µm in size (measured as circle-equivalent diameter CE; Figure 8). Overall, vesicular particles have lower *Vt*s than dense ones without an obvious link to their shape (see measurements of 2-D roughness and sphericity in Figure S8 in the supporting information). Our settling simulations using the 18 August 16:00 ADT wind field predict that vesicle-free particles 85–100 µm in size (depending on the sphericity) would reach the ground at the location of sample 44 if they were falling individually (Figure 6). We calculated *Vt* for these particles in sea level atmospheric conditions (comparable to *Vt* measured in the laboratory), which is ~0.4 m/s (Figure 8a). According to theory, particles with $Vt > 0.4$ m/s should have settled closer to the vent, while particles with $Vt < 0.4$ m/s should have settled farther away. The predominant grain size mode at ~100 µm (coarse grain size mode in Figure 8b) is consistent with the grain sizes expected to reach this distance as individual particles (Figure 8a), especially when considering variations in sphericity (Figure 8a) and particle density (Figure S6). Settling of particles in the grain size distribution mass-based mean (Folk & Ward, 1957) at ~24 µm requires accelerated sedimentation, which cannot be explained by changes in wind speed through time (see modeled *Vt* for sphericity 0.8 in the 19 August 04:00 ADT weak wind field in Figure 8a). These findings are consistent with the conclusions drawn from Figure 6, which show that individual settling can explain

only the sedimentation behavior of particles ≥100 μm. Below this threshold, the settling location of the particles is not controlled by the *Vt* of individual grains, from which we conclude that their size, shape and texture did not play a primary role in the sedimentation process.

6.4. Effect of the Bimodality of the Source Grain Size

While only a limited number of individual tephra samples show bimodality (Figures 3 and S1 in the supporting information), the TGSDs of both the August and September Mount Spurr fallout deposits are polymodal (Durant & Rose, 2009). The August TGSD has a coarse mode between 4 and 1 mm and a fine mode at 125 μm (Figure 3c), while the September TGSD has two coarse modes at 8 and 1 mm and a fine mode at 63 μm (Figure 3d). The coarse modes comprise grain sizes found within the first 50 km of the deposits (Figure 6). The fine mode of the August TGSD corresponds to the mean of the coarse grain size subpopulation found in the August ASMM, while the fine mode of the September TGSD corresponds to the mean of the unimodal grain size distributions found in the September ASMM (Figure 6). This suggests that the increased sedimentation at the ASMMs could have been generated, at least in part, by an overrepresentation of some grain sizes in the plume (i.e., the fine modes of the TGSDs). This could explain why the numerical simulations of the September eruption by Folch et al. (2010) produced an ASMM at about the right location without including aggregation. It is important to note, however, that TGSDs are reconstructed by weighting individual grain size distributions by the mass of tephra deposited close by (Durant & Rose, 2009). Consequently, local increases of MpuA that generate ASMMs may produce TGSD with an artificial overrepresentation of the grain sizes found in the ASMMs. That said, the distribution of sampling sites of the Spurr deposits (Figure 2) extends well outside of the ASMMs and thus supports the idea that the erupted TGSD, particularly the location and magnitude of the fine mode, should be considered in models of ash sedimentation.

The importance of the TGSD for tephra dispersion and sedimentation underlines the importance of understanding the mechanisms that generate polymodal source grain size distributions. At Spurr, the origin of the bimodality of the TGSD is not known. The fine modes are often related to a secondary process of fragmentation, such as comminution in pyroclastic density currents (PDCs) (Bernard & Le Pennec, 2016; Jones et al., 2016), which can produce significant fine ash enrichment in some fallout deposits (Bonadonna et al., 2002; Eychenne et al., 2012; Eychenne et al., 2015). The August and September eruptions, however, produced only small volume PDCs (<3 km runout distances) (Miller et al., 1995) and are thus unlikely sources of abundant fine ash. Another possibility is fine ash production by particle attrition during transport in the volcano conduit and the eruptive column, which can also generate a fine peak in TGSDs (Jones & Russell, 2017). We would expect attrition to create particles with sizes that are commensurate with textural heterogeneities of the pumice. The fine modes do not correspond, however, to the sizes of the phenocrysts or the microlites observed within lapilli and ash (Gardner et al., 1998; Riley et al., 2003), although the presence of two distinct pumice types (with varying crystallinity and vesicularity) suggests that the polymodality may arise from heterogeneities in the erupted magma. Additionally, seismicity accompanying the Spurr eruptions suggests relatively deep magma storage (~10 km) (Roman et al., 2004) and consequently the potential for protracted postfragmentation magma transport within the conduit.

6.5. Effect of Topography on Atmospheric Circulations

The locations of the Spurr ASMMs appear to be correlated with topography, with the local minima occurring on the windward flank of 2 km high mountain ranges and the maxima spreading across the leeward flank (Chugach Mountains in the August deposit and Talkeetna Mountains in September; Figures 2, 5a, and 5b). Directly upwind of both mountain ranges is the Cook Inlet Basin, where all tephra samples are extremely well sorted and lack particles finer than 125 μm (Figures 4 and 6). Sedimentation of fine ash starts at the foothills of the mountains (Figure 5), despite higher horizontal wind velocities in September than in August (Figure S3). These findings suggest a relationship between ash deposition and topography.

The mesoscale models of the atmospheric wind field (Figures 7 and S9 in the supporting information) highlight the importance of topography-induced atmospheric flow perturbations on the formation of ASMMs during the 1992 Spurr eruptions. Resulting vertical wind velocities of >1 m/s are significantly larger than *Vt*s of particles <100 μm (Figure 7); *Vt* measurements in sample 44 show that particles smaller than 140 μm have $Vt < 0.6$ m/s (Figure 8). This comparison suggests that these vertical wind variations can affect tephra settling. Along both plume trajectories (Figures 7c–7f and S9 in the supporting information), the

strongest oscillations of the vertical wind component are located above the complex topography of the mountain ranges. Such oscillations generate turbulence in the troposphere that can promote particle mixing and electrostatic aggregation of ash (Schumacher & Schmincke, 1995). Turbulence can also increase the *Vt* of individual small particles as a result of the effect of inertia on the interaction of the particles with turbulence in an ambient flow (Maxey, 1987; Maxey & Corrsin, 1986). These oscillations are stronger in more rapid wind fields (see August versus September vertical wind field; Figure 7). Efficient mixing may also aid hydrometeor development and facilitate en masse sedimentation due to hydrometeor sublimation (Durant & Rose, 2009). It can also promote entrainment of fine particles in the wakes of coarser grains (Lovell & Rose, 1991) and development of gravitational instabilities by maintaining concentrated clouds with limited sedimentation until they collapse and settle all particle sizes in particle-rich fingers (Carazzo & Jellinek, 2013). The correlation between the locations of these highly turbulent atmospheric zones (in relation to topography) and the location of enhanced deposition on the ground suggests that such processes were possible and helps to explain the wide range of particle sizes and *Vt*s found in the ASMMs (Figures 7 and S9c and S9d in the supporting information).

We conclude that topographically generated turbulence can accelerate the transfer of particles toward the low atmospheric layers (by mechanisms that include but are not limited to aggregation), where particle suspension or deposition is then strongly controlled by the atmospheric circulations. In fact, we note that 3-D simulations of the September plume dispersion and sedimentation (Folch et al., 2010) defined the atmosphere with a WRF model that accounts for complex topography, and therefore, that topographic effects may have added to the effects of the bimodal TGSD to produce the ASMM, even without aggregation.

7. Conclusion

The crosswind and downwind variations of mass and grain size within the 1992 August and September Mount Spurr fallout deposits indicate that the ASMMs did not result from preferential settling of fine ($<$100 μm) ash relative to coarser grain sizes. Moreover, aggregation processes usually invoked to explain the formation of ASMMs cannot satisfactorily explain their occurrence in the Spurr deposits. Simulations of individual but nonspherical particle settling through a homogeneous and horizontally stratified atmosphere indicates that enhanced settling at ASMMs affected the sedimentation of both fine ash and coarser particles. We show that the temporal variations of the wind field during eruption are not sufficient to generate the ASMMs. Measurement of the particle fall velocities in a sample from the August deposit shows that the texture and morphology of the particles had only a minor effect on settling within the ASMM. In contrast, the bimodality of the source grain size could have produced the ASMMs, as the fine modes correspond to the grain sizes found at these locations. We also observe a link between the deposit characteristics and the topography: in both deposits, the mass local minimum occurs across the windward flank of a 2 km high mountain range, while the local maximum (i.e., the ASMM) spreads across the leeward flank; both deposits also exhibit a change in sorting characteristics across the mountains. Mesoscale models of the three-dimensional wind field highlight the oscillations of the vertical wind field caused by topography; these oscillations can promote particle mixing, aggregation, and aid formation of hydrometeors and resulting deposition via gravitational instabilities and by wake capture.

Importantly, this work shows that the formation of ASMMs is not always directly related to processes of enhanced sedimentation of fine ash. The pronounced Spurr ASMMs are likely the consequence of a combination of factors, including the original polymodality of the TGSD and enhanced tephra sedimentation due to topography-induced perturbations of the wind field. Such topography effects may also play an important role in the formation and longevity of ash-hydrometeors and should be explored in relation to en masse sedimentation processes of volcanic plumes due to hydrometeor sublimation (Durant & Rose, 2009; Durant et al., 2009).

This work also highlights that using mass distributions in ASMMs to constrain aggregation processes without considering grain size characteristics (e.g., Folch et al., 2010; Mastin et al., 2016) may limit our understanding of the ensemble of processes that likely control ash sedimentation. We finally stress the value of combining particle transport modeling with detailed deposit observations, including not only mass depositional patterns on the ground but also detailed studies of grain shape, size, density, and, importantly, direct measurement of *Vt*s. Finally, we emphasize that including grain size—and not solely the mass—model evaluation of

fallout deposits is necessary to fully assess the quality of the sedimentation scheme. Recent modeling work has shown that such approach reduces the uncertainty on the simulation results (White et al., 2017).

Acknowledgments
J. Eychenne was funded by K. Cashman's AXA Research Fund and by a fellowship from the French National Research Institute for Sustainable Development (IRD). We thank Adam Durant and Game McGimsey for providing us with raw field and grain size data. We also thank Game McGimsey for providing information on the sampling campaigns and observations made in the field regarding aggregation. We thank Editor Michael Poland and two anonymous reviewers for detailed and constructive comments that greatly improved the quality of the manuscript. Data presented in this work are fully available in the main text and in the supporting information. This is Laboratory of Excellence ClerVolc contribution 271.

References

Bagheri, G., Rossi, E., Biass, S., & Bonadonna, C. (2016). Timing and nature of volcanic particle clusters based on field and numerical investigations. *Journal of Volcanology and Geothermal Research*, *327*, 520–530.

Beckett, F. M., Witham, C. S., Hort M., Stevenson, J. A., Bonadonna, C., & Millington, S. C. (2014). The sensitivity of NAME forecasts of the transport of volcanic ash clouds to the physical characteristics assigned to the particles. UK Met Office Forecasting Research Technical Report 592.

Beckett, F. M., Witham, C. S., Hort, M. C., Stevenson, J. A., Bonadonna, C., & Millington, S. C. (2015). Sensitivity of dispersion model forecasts of volcanic ash clouds to the physical characteristics of the particles. *Journal of Geophysical Research: Atmospheres*, *120*, 11,636–11,652. https://doi.org/10.1002/2015JD023609

Bellotti, F., Capra, L., Sarocchi, D., & D'Antonio, M. (2010). Geostatistics and multivariate analysis as a tool to characterize volcaniclastic deposits: Application to Nevado de Toluca volcano, Mexico. *Journal of Volcanology and Geothermal Research*, *191*(1–2), 117–128.

Bernard, J., & Le Pennec, J.-L. (2016). The milling factory: Componentry-dependent fragmentation and fines production in pyroclastic flows. *Geology*, *44*(11), 907–910.

Bonadonna, C., Mayberry, G. C., Calder, E. S., Sparks, R. S. J., Choux, C., Jackson, P., … Young, S. R. (2002). Tephra fallout in the eruption of Soufriere Hills Volcano, Montserrat. *Geological Society, London, Memoirs*, *21*(1), 483–516.

Bonadonna, C., & Phillips, J. C. (2003). Sedimentation from strong volcanic plumes. *Journal of Geophysical Research 108*(B7), 2340. https://doi.org/10.1029/2002JB002034

Brazier, S., Sparks, R. S. J., Carey, S. N., Sigurdsson, H., & Westgate, J. A. (1983). Bimodal grain size distribution and secondary thickening in air-fall ash layers. *Nature*, *301*, 115–119.

Brown, P. P., & Lawler, D. F. (2003). Sphere drag and settling velocity revisited. *Journal of Environmental Engineering-Asce*, *129*(3), 222–231.

Brown, R. J., Bonadonna, C., & Durant, A. J. (2012). A review of volcanic ash aggregation. *Physics and Chemistry of the Earth, Parts A/B/C*, *45–46*, 65–78.

Bursik, M. I., Sparks, R. S. J., Gilbert, J. S., & Carey, S. N. (1992). Sedimentation of tephra by volcanic plumes: I. Theory and its comparison with a study of the Fogo A plinian deposit, Sao Miguel (Azores). *Bulletin of Volcanology*, *54*(4), 329–344.

Caballero, L., Sarocchi, D., Soto, E., & Borselli, L. (2014). Rheological changes induced by clast fragmentation in debris flows. *Journal of Geophysical Research: Earth Surface*, *119*, 1800–1817. https://doi.org/10.1002/2013JF002942

Carazzo, G., & Jellinek, A. M. (2012). A new view of the dynamics, stability and longevity of volcanic clouds. *Earth and Planetary Science Letters*, *325–326*, 39–51.

Carazzo, G., & Jellinek, A. M. (2013). Particle sedimentation and diffusive convection in volcanic ash-clouds. *Journal of Geophysical Research: Solid Earth*, *118*, 1420–1437. https://doi.org/10.1002/jgrb.50155

Carey, S. N., & Sigurdsson, H. (1982). Influence of particle aggregation on deposition of distal tephra from the May 18, 1980, eruption of Mount St. Helens volcano. *Journal of Geophysical Research*, *87*, 7061–7072. https://doi.org/10.1029/JB087iB08p07061

Cashman, K., & Rust, A. (2016). Volcanic ash—Generation and spatial variations. In S. Mackie, et al. (Eds.), *Volcanic ash: Hazard observation* (pp. 5–22). Elsevier.

Clark, T. L. (2003). Block-iterative method of solving the non-hydrostatic pressure in terrain-following coordinates: Two-level pressure and truncation error analysis. *Journal of Applied Meteorology*, *42*, 970–983.

Clark, T. L., Hall, W. D., & Coen, J. L. (1996). Source code documentation for the Clark-Hall Cloud-scale model: Code version G3CH01, The National Center for Atmospheric Research (NCAR) Technical Note. p. 174.

Clark, T. L., Hall, W. D., Kerr, R. M., Middleton, D., Radke, L., Ralph, F. M., … Levinson, D. (2000). Origins of aircraft-damaging clear-air turbulence during the 9 December 1992 Colorado downslope windstorm: Numerical simulations and comparison with observations. *Journal of the Atmospheric Sciences*, *57*(8), 1105–1131.

Coen J. L. (2013). *Modeling wildland fires: A description of the coupled atmosphere-wildland fire environment model (CAWFE)* (NCAR Technical Notes NCAR/TN-500 +STR). Boulder, CO: National Center for Atmospheric Research. Retrieved from http://doi.org/10.5065/D6K64G2G

Cornell, W., Carey, S., & Sigurdsson, H. (1983). Computer simulation of transport and deposition of the campanian Y-5 ash. *Journal of Volcanology and Geothermal Research*, *17*(1–4), 89–109.

Costa, A., Folch, A., & Macedonio, G. (2010). A model for wet aggregation of ash particles in volcanic plumes and clouds: 1. Theoretical formulation. *Journal of Geophysical Research*, *115*, B09201. https://doi.org/10.1029/2009JB007175

Del Bello, E., Taddeucci, J., de Michieli Vitturi, M., Scarlato, P., Andronico, D., Scollo, S., … Ricci, T. (2017). Effect of particle volume fraction on the settling velocity of volcanic ash particles: insights from joint experimental and numerical simulations. *Scientific Reports*, *7*, 39620.

Di Muro, A., Rosi, M., Aguilera, E., Barbieri, R., Massa, G., Mundula, F., & Pieri, F. (2008). Transport and sedimentation dynamics of transitional explosive eruption columns: The example of the 800 BP Quilotoa plinian eruption (Ecuador). *Journal of Volcanology and Geothermal Research*, *174*(4), 307–324.

Durant, A. J., & Rose, W. I. (2009). Sedimentological constraints on hydrometeor-enhanced particle deposition: 1992 Eruptions of Crater Peak, Alaska. *Journal of Volcanology and Geothermal Research*, *186*(1–2), 40–59.

Durant, A. J., Rose, W. I., Sarna-Wojcicki, A. M., Carey, S., & Volentik, A. C. M. (2009). Hydrometeor-enhanced tephra sedimentation: Constraints from the 18 May 1980 eruption of Mount St. Helens. *Journal of Geophysical Research*, *114*, B03204. https://doi.org/10.1029/2008JB005756

Durant, A. J., Shaw, R. A., Rose, W. I., Mi, Y., & Ernst, G. G. J. (2008). Ice nucleation and overseeding of ice in volcanic clouds. *Journal of Geophysical Research: Atmospheres*, *113*, D09206. https://doi.org/10.1029/2007JD009064

Eckermann, S. D., & Preusse, P. (1999). Global measurements of stratospheric mountain waves from space. *Science*, *286*(5,444), 1534–1537.

Engwell, S. L., & Eychenne, J. (2016). Contribution of fine ash to the atmosphere from plumes associated with pyroclastic density currents. In S. Mackie, et al. (Eds.), *Volcanic ash: Hazard observation* (pp. 67–85). Elsevier.

Eychenne, J., & Pennec, J.-L. (2012). Sigmoidal particle density distribution in a subplinian scoria fall deposit. *Bulletin of Volcanology*, *74*(10), 2243–2249.

Eychenne, J., Cashman, K. V., Rust, A. C., & Durant, A. (2015). Impact of the lateral blast on the spatial pattern and grain size characteristics of the May 18, 1980 Mount St. Helens fallout deposit. *Journal of Geophysical Research*, *120*, 6018–6038. https://doi.org/10.1002/2015JB012116

Eychenne, J., Pennec, J.-L., Troncoso, L., Gouhier, M., & Nedelec, J.-M. (2012). Causes and consequences of bimodal grain-size distribution of tephra fall deposited during the August 2006 Tungurahua eruption (Ecuador). *Bulletin of Volcanology*, *74*(1), 187–205.
Folch, A., Costa, A., Durant, A., & Macedonio, G. (2010). A model for wet aggregation of ash particles in volcanic plumes and clouds: 2. Model application. *Journal of Geophysical Research*, *115*, B09202. https://doi.org/10.1029/2009JB007176
Folk, R. L., & Ward, W. C. (1957). Brazos River Bar: A study of the significance of grain size parameters. *Journal of Sedimentary Petrology*, *27*, 3–26.
Ganser, G. H. (1993). A rational approach to drag prediction of spherical and nonspherical particles. *Powder Technology*, *77*(2), 143–152.
Gardner, C. A., Cashman, K. V., & Neal, C. A. (1998). Tephra-fall deposits from the 1992 eruption of Crater Peak, Alaska: implications of clast textures for eruptive processes. *Bulletin of Volcanology*, *59*, 537–555.
Gilbert, J. S., & Lane, S. J. (1994). The origin of accretionary lapilli. *Bulletin of Volcanology*, *56*(5), 398–411.
Hildreth, W., & Drake, R. E. (1992). Volcan Quizapu, Chilean Andes. *Bulletin of Volcanology*, *54*, 63–125.
Horwell, C., & Baxter, P. (2006). The respiratory health hazards of volcanic ash: A review for volcanic risk mitigation. *Bulletin of Volcanology*, *69*, 1–24.
James, M. R., Gilbert, J. S., & Lane, S. J. (2002). Experimental investigation of volcanic particle aggregation in the absence of a liquid phase. *Journal of Geophysical Research 107*(B9), 2191. https://doi.org/10.1029/2001JB000950
James, M. R., Lane, S. J., & Gilbert, J. S. (2003). Density, construction, and drag coefficient of electrostatic volcanic ash aggregates. *Journal of Geophysical Research 108*(B9), 2435. https://doi.org/10.1029/2002JB002011
Jenkins, S. F., Wilson, T. M., Magill, C., Miller, V., Stewart, C., Blong, R., … Costa, A. (2015). Volcanic ash fall hazard and risk. In S. C. Loughlin, et al. (Eds.), *Global volcanic hazard and risk* (pp. 173–221). Cambridge: Cambridge University Press.
Jiang, Q., & Doyle, J. D. (2004). Gravity wave breaking over the central Alps: Role of complex terrain. *Journal of the Atmospheric Sciences*, *61*(18), 2249–2266.
Jones, T. J., & Russell, J. K. (2017). Ash production by attrition in volcanic conduits and plumes. *Scientific Reports*, *7*(1), 5538.
Jones, T. J., McNamara, K., Eychenne, J., Rust, A. C., Cashman, K. V., Scheu, B., & Edwards, R. (2016). Primary and secondary fragmentation of crystal-bearing intermediate magma. *Journal of Volcanology and Geothermal Research*, *327*, 70–83.
Kueppers, U., Cimarelli, C., Hess, K.-U., Taddeucci, J., Wadsworth, F., & Dingwell, D. (2014). The thermal stability of Eyjafjallajokull ash versus turbine ingestion test sands. *Journal of Applied Volcanology*, *3*(1), 4.
Larsson, W. (1937). Vulkanische Asche vom Ausbruch des chilenischen Vulkans Quizapu (1932) in Argentina gesammelt. *Geollogical Institution Upsala Bullettin*, *26*, 27–52.
Lovell, C. J., & Rose, C. W. (1991). Wake-capture effects observed in a comparison of methods to measure particle settling velocity beyond Stokes' range. *Journal of Sedimentary Research*, *61*, 575–582.
Manzella, I., Bonadonna, C., Phillips, J. C., & Monnard, H. (2015). The role of gravitational instabilities in deposition of volcanic ash. *Geology*, *43*, 211–214.
Mastin, L. G., van Eaton, A. R., & Durant, A. J. (2016). Adjusting particle-size distributions to account for aggregation in tephra-deposit model forecasts. *Atmospheric Chemistry and Physics*, *16*(14), 9399–9420.
Maxey, M. R. (1987). The gravitational settling of aerosol particles in homogeneous turbulence and random flow fields. *Journal of Fluid Mechanics*, *174*, 441–465.
Maxey, M. R., & Corrsin, S. (1986). Gravitational settling of aerosol particles in randomly oriented cellular flow fields. *Journal of the Atmospheric Sciences*, *43*(11), 1112–1134.
McGimsey, R. G., Neal, C. A., & Riley, C. M. (2001). Areal distribution, thickness, mass, volume and grain size of tephra-fall deposits from the 1992 eruptions of Crater Peak vent, Mt. Spurr Volcano, Alaska. U.S. Geological Survey Open-File Report 01–370.
Miller, T. P., Neal, C. A., & Waitt, R. B. (1995). Pyroclastic flows of the 1992 Crater Peak eruptions: Distribution and origin. In T. E. C. Keith (Ed.), *The 1992 eruptions of Crater Peak vent, Mount Spurr volcano, Alaska* (*USGS Bulletin 2139*) (pp. 81–88). Washington, DC: U.S. Geological Society.
Neal, C. A., McGimsey, R. G., Gardner, C. A., Harbin, M. L., & Nye, C. J. (1995). Tephra-fall deposits from the 1992 eruptions of Crater Peak, Mount Spurr Volcano, Alaska: A preliminary report on distribution, stratigraphy, and composition. In T. E. C. Keith (Ed.), *The 1992 eruptions of Crater Peak vent, Mount Spurr volcano, Alaska* (*U.S. Geological Society Bulletin 2139*) (pp. 65–80). Washington, DC: U.S. Geological Society.
Poulidis, A. P., Takemi, T., Iguchi, M., & Renfrew, I. A. (2017). Orographic effects on the transport and deposition of volcanic ash: A case study of Mt. Sakurajima, Japan. *Journal of Geophysical Research: Atmospheres*, *122*, 9332–9350. https://doi.org/10.1002/2017JD026595
Pyle, D. M. (1989). The thickness, volume and grainsize of tephra fall deposits. *Bulletin of Volcanology*, *51*, 1–15.
Riley, C. M., Rose, W. I., & Bluth, G. J. S. (2003). Quantitative shape measurements of distal volcanic ash. *Journal of Geophysical Research 108*(B10), 2504. https://doi.org/10.1029/2001JB000818
Roman, D. C., Moran, S. C., Power, J. A., & Cashman, K. V. (2004). Temporal and spatial variation of local stress fields before and after the 1992 eruptions of Crater Peak Vent, Mount Spurr Volcano, Alaska. *Bulletin of the Seismological Society of America*, *94*(6), 2366–2379.
Rose, W., & Durant, A. (2009). Fine ash content of explosive eruptions. *Journal of Volcanology and Geothermal Research*, *186*, 32–39.
Rose, W., Bluth, G. J. S., Schneider, D., Ernst, G., Riley, C. M., Henderson, L. J., & McGimsey, R. G. (2001). Observations of volcanic clouds in their first few days of atmospheric residence: The 1992 eruptions of Crater Peak, Mount Spurr Volcano, Alaska. *The Journal of Geology*, *109*(6), 677–694.
Rose, W. I., & Durant, A. J. (2011). Fate of volcanic ash: Aggregation and fallout. *Geology*, *39*(9), 895–896.
Rose, W. I., Kostinski, A., & Kelley, L. (1995). Real-time C-band radar observations of 1992 eruption clouds from Crater Peak, Mount Spurr Volcano, Alaska. In T. E. C. Keith (Ed.), *The 1992 eruptions of Crater Peak vent, Mount Spurr volcano, Alaska* (*U.S. Geological Society Bulletin 2139*) (pp. 19–26). Washington, DC: U.S. Geological Society.
Sarna-Wojcicki, A., Shipley, S., Waitt, R. B., Dzurisin, D., & Wood, S. (1981). Aeral distribution, thickness, mass, volume and grain size of air-fall ash from the six major eruptions of 1980. *U.S. Geological Survey Professional Paper*, *1250*, 577–600.
Scasso, R. A., Corbella, H., & Tiberi, P. (1994). Sedimentological analysis of the tephra from the 12–15 August 1991 eruption of Hudson volcano. *Bulletin of Volcanology*, *56*(2), 121–132.
Schneider, D., Rose, W. I., & Kelley, L. (1995). Tracking of 1992 eruption clouds from Crater Peak Vent of Mount Spurr Volcano, Alaska, using AVHRR. In T. E. C. Keith (Ed.), *The 1992 eruptions of Crtaer Peak vent, Mount Spurr volcano, Alaska* (*U.S. Geological Society Bulletin 2139*) (pp. 27–36). Washington, DC: U.S. Geological Society.
Schumacher, R., & Schmincke, H.-U. (1995). Models for the origin of accretionary lapilli. *Bulletin of Volcanology*, *56*(8), 626–639.
Sorem, R. K. (1982). Volcanic ash clusters: Tephra rafts and scavengers. *Journal of Volcanology and Geothermal Research*, *13*(1–2), 63–71.
Sparks, R. S. J., Bursik, M. I., Ablay, G. J., Thomas, R. M. E., & Carey, S. N. (1992). Sedimentation of tephra by volcanic plumes. Part 2: Controls on thickness and grain-size variations of tephra fall deposits. *Bulletin of Volcanology*, *54*(8), 685–695.

Taddeucci, J., Scarlato, P., Montanaro, C., Cimarelli, C., Del Bello, E., Freda, C., … Dingwell, D. B. (2011). Aggregation-dominated ash settling from the Eyjafjallajokull volcanic cloud illuminated by field and laboratory high-speed imaging. *Geology*, *39*(9), 891–894.

Thielen, J., Wobrock, W., Gadian, A., Mestayer, P., & Creutin, J.-D. (2000). The possible influence of urban surfaces on rainfall development: A sensitivity study in 2D in the meso-γ-scale. *Atmospheric Research*, *54*(1), 15–39.

Van Eaton, A., Muirhead, J., Wilson, C. N., & Cimarelli, C. (2012). Growth of volcanic ash aggregates in the presence of liquid water and ice: An experimental approach. *Bulletin of Volcanology*, *74*(9), 1963–1984.

Walker, G. P. L. (1981). Generation and dispersal of fine ash and dust by volcanic eruptions. *Journal of Volcanology and Geothermal Research*, *11*(1), 81–92.

Watanabe, K., Ono, K., Sakaguchi, K., Takada, A., & Hoshizumi, H. (1999). Co-ignimbrite ash-fall deposits of the 1991 eruptions of Fugen-dake, Unzen Volcano, Japan. *Journal of Volcanology and Geothermal Research*, *89*(1–4), 95–112.

Watt, S. F. L., Gilbert, J. S., Folch, A., Phillips, J. C., & Cai, X. M. (2015). An example of enhanced tephra deposition driven by topographically induced atmospheric turbulence. *Bulletin of Volcanology*, *77*(5), 1–14.

Watt, S. F. L., Pyle, D. M., Mather, T. A., Martin, R. S., & Matthews, N. E. (2009). Fallout and distribution of volcanic ash over Argentina following the May 2008 explosive eruption of Chaitén, Chile. *Journal of Geophysical Research*, *114*, B04207. https://doi.org/10.1029/2008JB006219

Webley, P. W. (2015). Volcanoes and the aviation industry. In S. C. Loughlin, et al. (Eds.), *Global volcanic hazards and risk* (pp. 295–298). Cambridge: Cambridge University Press.

White, J. T., Connor, C. B., Connor, L., & Hasenaka, T. (2017). Efficient inversion and uncertainty quantification of a tephra fallout model. *Journal of Geophysical Research: Solid Earth*, *122*, 281–294. https://doi.org/10.1002/2016JB013682

Wiesner, M. G., Wetzel, A., Catane, S. G., Listanco, E. L., & Mirabueno, H. T. (2004). Grain size, areal thickness distribution and controls on sedimentation of the 1991 Mount Pinatubo tephra layer in the South China Sea. *Bulletin of Volcanology*, *66*(3), 226–242.

Wilson, T. M., Jenkins, S. F., & Stewart, C. (2015). Volcanic ash fall impact. In S. C. Loughlin, et al. (Eds.), *Global volcanic hazards and risk* (pp. 281–288). Cambridge: Cambridge University Press.

Wobrock, W., Flossmann, A. I., Monier, M., Pichon, J.-M., Cortez, L., Fournol, J.-F., … Laj, P. (2001). The Cloud Ice Mountain Experiment (CIME) 1998: Experiment overview and modelling of the microphysical processes during the seeding by isentropic gas expansion. *Atmospheric Research*, *58*(4), 231–265.

Wright, H. M. N., Cashman, K., Mothes, P. A., Hall, M. L., Ruiz, G. A., & Le Pennec, J. L. (2012). Estimating rates of decompression from textures of erupted ash particles produced by 1999–2006 eruptions of Tungurahua volcano, Ecuador. *Geology*, *40*(7), 619–622.